Electrochimica Acta 437 (2023) 141521

Contents lists available at ScienceDirect

Electrochimica Acta

journal homepage: www.journals.elsevier.com/electrochimica-acta

Spray-deposited cobalt-doped RuO_2 electrodes for high-performance supercapacitors

Chandrashekhar R, Abhijit A. Yadav *

Thin Film Physics Laboratory, Department of Physics, Electronics and Photonics, Rajarshi Shahu Mahavidyalaya (Autonomous), Latur, Maharashtra 413512, India

ARTICLE INFO

Keywords:
Spray pyrolysis
Ruthenium oxide
Aqueous/organic solvent mixture
Supercapacitor
Cyclic voltammetry

ABSTRACT

RuO_2 is widely used as the material in supercapacitors; however, there is little information on the doping RuO_2 with cobalt using an aqueous/organic solvent mixture in the spray pyrolysis technique. The phase purity and rutile crystal structure of cobalt-doped RuO_2 were validated using X-ray diffraction. Optical studies indicated that the bandgap can be decreased from 1.80 eV to 1.70 eV by doping the RuO_2 with cobalt. In this study, the performance of electrochemical supercapacitors and their morphology are both significantly altered by cobalt doping. 1.00 mol% cobalt-doped RuO_2 displays a high specific capacitance (1072 F g^{-1} at a 5 mV s^{-1} scan rate) compared with that of undoped RuO_2 (893 F g^{-1} at a 5 mV s^{-1} scan rate). 1.00 mol% cobalt-doped RuO_2 had the highest specific energy (96.02 W h kg^{-1}) at a specific power value of 1.702 kW kg^{-1}. The specific capacitance was improved (1158 F g^{-1} at 0.5 A g^{-1}) in a 0.5 M H_2SO_4 electrolyte. After 1000 charge–discharge cycles, 94% of the capacity of a 1.00 mol% cobalt-doped RuO_2 electrode was preserved, indicating outstanding long-term cyclic stability. This study endorses the view that 1.00 mol% cobalt-doped RuO_2 is a promising material for supercapacitor applications.

1. Introduction

Currently, more than 80% of the energy used in the world comes from fossil fuels. Because this fossil fuel use is contributing to the greenhouse effect and fossil fuel reserves are getting exhausted, the production of electrical energy from sustainable and renewable sources, including the sun, winds, and tides, is increasing [1,2]. Because of the erratic nature of the sun and winds, energy-conversion and energy-storage devices, including batteries/fuel cells and supercapacitors, are receiving a lot of interest. It is well known that supercapacitors work in conjunction with other energy storage/generating devices such as batteries and fuel cells [3]. Supercapacitors are used in computers, wearable electronics, video cameras, mobile phones, transmitters, backup power supplies, hybrid electric vehicles, etc [4–8]. Supercapacitors are classified on the basis of the charge-storage process as electric double-layer capacitors, pseudocapacitors and hybrid supercapacitors. Conducting polymers, carbon and metal oxides/hydroxides are commonly utilised supercapacitor electrode materials. The specific capacitance of metal oxides is relatively high [5,6,9].

The morphology, electrical conductivity, and crystal structure of an electrode material govern a supercapacitor's electrochemical performance. Numerous metal oxides, including ruthenium oxide (RuO_2), Hausmannite (Mn_3O_4), manganese dioxide (MnO_2), nickel oxide (NiO), nickel hydroxide ($Ni(OH)_2$), cobalt oxide (Co_3O_4), cobalt hydroxide ($Co(OH)_2$), iron oxides (Fe_3O_4 (magnetite) and Fe_2O_3 (hematite)), titanium oxide (TiO_2), tin oxide (SnO_2), vanadium oxide (V_2O_5), nickel cobalt oxide ($NiCo_2O_4$), nickel ferrite ($NiFe_2O_4$), cobalt ferrite ($CoFe_2O_4$), and copper oxide (CuO), have been comprehensively studied for use as supercapacitor electrodes [9–13]. RuO_2/hydrous RuO_2 has been extensively studied because it has exceptional qualities, including a high electrical conductivity of 10^5 $(\Omega\ cm)^{-1}$ and a theoretical capacitance of 1300–2200 F g^{-1} [14].

The ionic and electrical conductivities, specific capacitance and cycle stability of metal oxides can be enhanced by doping them with different elements [15]. Hasan and coworkers [16] explored the electrochemical characteristics of sol–gel synthesized Ni-doped $ZnMn_2O_4$. They found that the material had a specific capacitance of 161.3 F g^{-1}. Kishor and colleagues [17] electrodeposited Cu-doped RuO_2 electrocatalysts and studied their selectivity and specific chlorine evolution reaction activity. Joshi and Sutrave [18] prepared Mn-doped RuO_2 electrodes using the sol–gel process. The Mn doping had significant effects on the pore size of the electrodes. The specific capacitance was highest (328 F g^{-1}) with 1at

* Corresponding author.
E-mail address: aay_physics@yahoo.co.in (A.A. Yadav).

https://doi.org/10.1016/j.electacta.2022.141521
Received 28 August 2022; Received in revised form 16 October 2022; Accepted 9 November 2022
Available online 12 November 2022

% Mn doping. Macounová et al. [19] prepared Co-, Mg-, Ni- and Zn-doped RuO_2 electrodes using a spray-freezing/freeze-drying method. Petrykin and coworkers [20] prepared Co-doped RuO_2 electrocatalysts using the co-precipitation method. It has been reported that the chlorine and oxygen evolution reaction activities are substantially improved by cobalt doping. Su et al. [21] described the preparation of ultra-small nanocrystals of Cu-doped RuO_2. An improvement in oxygen evolution reaction activity with Cu doping was noted.

A survey of the literature indicates that most doped RuO_2 materials are utilized as electrocatalysts for hydrogen evolution and oxygen evolution reactions [22,23]. Very few reports are available on spray-deposited doped RuO_2 prepared using aqueous/organic solvent mixtures. Such mixtures were used to spray-deposit cobalt-doped RuO_2 electrodes with various levels of cobalt. The electrodes with 1.00 mol% cobalt exhibited the best electrochemical properties, including a specific capacitance value of 1072 F g^{-1} and a stability of 94.04% after 1000 charge–discharge cycles. These findings indicate that doping RuO_2 with cobalt improves the electrochemical performance by increasing the active surface area.

2. Experimental

2.1. Materials

AR-grade cobalt chloride hexahydrate ($CoCl_2.6H_2O$) and ruthenium (III) chloride trihydrate ($RuCl_3 \bullet 3H_2O$) were used as precursors to spray-deposit cobalt-doped RuO_2 electrodes with different cobalt contents. The cobalt content in the precursor solution ($CoCl_2.6H_2O$) was varied to obtain 0.25 mol%, 0.50 mol%, 0.75 mol%, 1.00 mol%, 1.25 mol%, 1.50 mol%, 1.75 mol% and 2.00 mol% cobalt-doped RuO_2 electrodes, this was considered as stock solution. Ten ml of this stock solution was mixed with 10 ml of ethanol to make final spraying solution 20 ml. The optimized values of the preparative parameters were the following: substrate temperature, 290°C; precursor solution concentration, 50 mM; spray rate, 3–4 ml min^{-1}; nozzle-to-substrate distance, 28 cm; carrier gas (air) pressure, 176 kPa.

2.2. Characterization methods

The crystal structure of the cobalt-doped RuO_2 electrodes was studied using Cu-Kα radiation (λ = 1.5406 Å) from an X-ray diffractometer (Ultima IV). The 2θ values obtained were in the range 10–80° (step size 0.02°). A Field emission scanning electron microscopy (FESEM) (S-4800) was used to carry out morphological analyses of the electrodes. The absorption spectra of the cobalt-doped RuO_2 electrodes were plotted to determine the optical bandgap using a UV–visible spectrophotometer (Ocean Optics JAZ-3 and NIR-QUEST). Electrical resistivity measurements of the cobalt-doped RuO_2 electrodes were made using the four-point probe measurement technique (Vander paw configuration) at constant current (Source Measurement Unit-Keithley 2450 SMU). Electrochemical measurements including cyclic voltammetry (CV), galvanostatic charge-discharge (GCD) and electrochemical impedance spectroscopy (EIS) were made using an electrochemical analyzer (CHI 608D). A typical three-electrode cell arrangement was used, with a 1 cm^2 cobalt doped RuO_2 film as the working electrode and saturated Ag/AgCl and platinum as the reference and counter electrodes in a 0.5 M H_2SO_4 electrolyte. The electrochemical impedance was measured at open circuit potential in a frequency range of 100 kHz to 1 Hz, with an AC amplitude of 5 mV.

3. Results and discussion

3.1. Specific capacitance

Fig. 1 shows the variation of specific capacitance (at 10 mV s^{-1}) with cobalt doping. It can be observed that the specific capacitance of the electrodes rises with the doping level from a value of 813 F g^{-1} for undoped rutile RuO_2. It reaches a maximum value (992 F g^{-1}) at 1.00 mol% cobalt doping. It decreases when the cobalt doping is increased above 1.00 mol%, with the value at 2.00 mol% being 938 F g^{-1}. The variation in the specific capacitance is related to the changes in electrical resistivity of the cobalt-doped RuO_2 electrodes. The maximum specific capacitance obtained with 1.00 mol% cobalt doping in RuO_2 electrodes may be due to optimal doping of cobalt at 1.00 mol% than other doping contents in RuO_2.

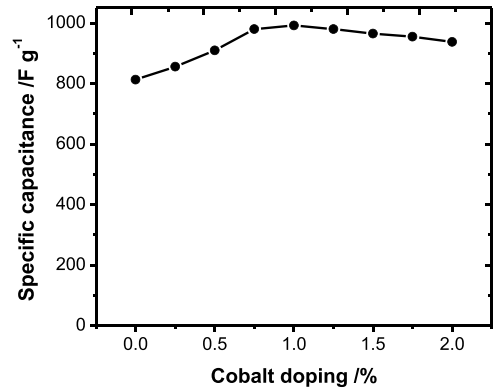

Fig. 1. Variation of specific capacitance (at 10 mVs^{-1}) with cobalt doping in RuO_2.

3.2. X-ray diffraction (XRD)

The lattice structure and related factors of the cobalt-doped RuO_2 electrodes were studied using XRD. As can be seen in Fig. 2, the XRD patterns of the electrodes show a polycrystalline crystal structure irrespective of the cobalt content. The major diffraction peaks of the undoped and cobalt-doped RuO_2 electrodes are present at around 28.06°, 35.09°, 40.10°, 54.33° and 65.65°, corresponding to the (110), (101), (200), (211) and (310) planes of rutile RuO_2 (JCPDS card no. 88-0322). It can be seen from Table 1 that both the undoped and cobalt-doped RuO_2 exhibit a rutile tetragonal crystal structure with the space group P42 [24]. This is supported by an agreement between the observed spacing and the standard interplanar spacing of the (hkl) planes. The (110) peak intensity increases with increasing cobalt doping content up to 1.00 mol% and decreases thereafter. This is because the alignment of fine grains along the (110) direction grows stronger up to 1.00 mol%, resulting in an enhancement of the peak intensity. The decrease in peak intensity above 1.00 mol% might be due to fluctuations in the electron density or due to the presence of point defects [25].

The XRD patterns do not show any diffraction peaks corresponding

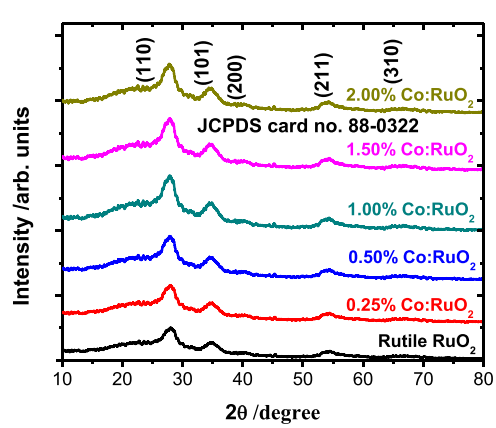

Fig. 2. XRD patterns of Rutile and cobalt-doped RuO_2 electrodes.

Table 1
Structural data for cobalt doped RuO_2 spray deposited with various cobalt-doping contents.

Cobalt doping content (mol %)	2θ (°)	d (Å) (Cal.)	d (Å) (Std.)	hkl	a (Å)	c (Å)	D (nm)
Undoped	27.98	3.186	3.177	110	4.500	3.175	13
	34.54	2.594	2.555	101			
	40.08	2.248	2.247	200			
	54.24	1.690	1.687	211			
	65.96	1.415	1.421	310			
0.25	27.89	3.196	3.177	110	4.511	3.181	12
	34.47	2.599	2.555	101			
	40.02	2.251	2.247	200			
	53.92	1.699	1.687	211			
	66.03	1.414	1.421	310			
0.50	27.76	3.211	3.177	110	4.514	3.188	11
	34.41	2.604	2.555	101			
	40.15	2.244	2.247	200			
	53.87	1.700	1.687	211			
	65.98	1.415	1.421	310			
1.00	27.72	3.215	3.177	110	4.519	3.190	10
	34.38	2.606	2.555	101			
	40.11	2.246	2.247	200			
	54.21	1.690	1.687	211			
	66.02	1.414	1.421	310			
1.50	27.70	3.217	3.177	110	4.522	3.189	9
	34.38	2.606	2.555	101			
	40.10	2.247	2.247	200			
	53.83	1.701	1.687	211			
	65.98	1.415	1.421	310			
2.00	27.68	3.220	3.177	110	4.573	3.176	9
	34.35	2.608	2.555	101			
	39.20	2.296	2.247	200			
	53.73	1.704	1.687	211			
	65.98	1.415	1.421	310			

2θ; Bragg's angle, d; interplanar spacing, hkl; Miller indices, 'a' and 'c'; lattice constants, D; crystallite size.

to CoO, Co_2O_3 or Co_3O_4 confirming that cobalt atoms are substituted in RuO_2 lattice. Interestingly, the shifting of (110) peak belonging to RuO_2 towards the lower 2θ side with increasing cobalt doping content indicates that cobalt atoms have been effectively substituted in the RuO_2 lattice. The difference in the ionic radii of the cobalt and ruthenium ions causes the crystalline RuO_2 lattice to swell, resulting in the shifting of the XRD peaks to the lower 2θ side after doping, and this is compatible with Bragg's equation [25]. The changes in the position of the (110) peak with changes in cobalt doping are related to changes in the microstructure of the RuO_2 electrodes, which affect the supercapacitive behaviour, as will be seen in subsequent sections (electrochemical studies) [15]. Similar observations related to the structure of cobalt-doped RuO_2 were reported by Petrykin et al. [20].

The crystallite sizes of the cobalt-doped RuO_2 electrodes corresponding to the (110) plane were determined using the Debye-Scherrer equation [26]. The crystallite size decreases as the cobalt content increases, and it is estimated to be in the range 13–9 nm. The decrease in crystallite size is due to replacement of Ru^{3+} ions (ionic radius 0.82 Å) with Co^{2+} (ionic radius 0.885 Å). The alteration/increase in ionic radius produces lattice distortions, increasing the FWHM and decreasing the crystallite size [27]. Abbott and colleagues [28] have reported similar results for Mg-doped RuO_2.

3.3. FESEM

Fig. 3 (a)-(e) shows the FESEM images (magnification 200,000 ×) of cobalt-doped RuO_2 electrodes with different cobalt content. The undoped RuO_2 electrode shows a porous morphology, with larger particles formed by controlled agglomeration of smaller particles (Fig. 3 (a)). There is a smooth and homogeneous surface with compact grains in the electrode with 0.25 mol% cobalt (Fig. 3 (b)). The porosity and homogeneity of the RuO_2 electrodes increase with increasing cobalt-doping content in the RuO_2 (Fig. 3 (c)-(e)). The porous structure promotes the contact between the electrolyte ions and the RuO_2 working electrode. The FESEM images in Fig. 3 (a)–(e) shows that the cobalt doping obviously changes the microstructure of the RuO_2 electrodes, improving their supercapacitive behaviour. A similar porous morphology has been reported by Yang and colleagues [29] for RuO_2/RGOH prepared using the hydrothermal method and by Lenar and coworkers [30] for RuO_2 nanoparticles.

3.4. Optical

Optical absorption spectra were recorded in the wavelength range 350–1050 nm to compare the bandgaps of RuO_2 electrodes with different cobalt-doping content. The electrodes had a high coefficient of absorption, 10^4 cm^{-1}. A Tauc plot, a graph with $(\alpha h\nu)^2$ plotted against $h\nu$ (Fig. 4 (a)), was utilised to estimate the optical bandgap of the undoped and cobalt-doped electrodes [31]. The estimated bandgap values of RuO_2 electrodes with different cobalt-doping levels are provided in Table 2. Fig. 4 (b) shows the variation of the bandgap with cobalt-doping content. The optical bandgap of a spray-deposited undoped RuO_2 electrode was 1.80 eV. With 0.25 mol%, 0.50 mol%, 1.00 mol%, 1.50 mol% and 2.00 mol% cobalt doping, the optical bandgap became 1.77 eV, 1.75 eV, 1.73 eV, 1.71 eV and 1.7 eV, respectively. The reduction in bandgap with increasing cobalt-doping level is due to the band tailing effect and an increase in acceptor density [32]. The decrease in bandgap with increasing cobalt-doping level confirms that cobalt ions are continuously substituted in the RuO_2 lattice. Also, the localized defects created in the RuO_2 by oxygen vacancies due to the cobalt doping significantly decrease the bandgap [33]. The bandgap values estimated in this work are in agreement with results reported in the literature for RuO_2 [34–36].

3.5. Electrical

The four-probe technique was used to evaluate the contact resistances for spray-deposited cobalt-doped RuO_2 and the results are shown in Fig. 5(a). The lowest electrical resistance is witnessed for 1.00 mol% cobalt-doped RuO_2 electrode. The variation of electrical resistivities with inverse of absolute temperature (1000/T) for spray-deposited RuO_2 electrodes with different cobalt-doping levels is shown in Fig. 5 (b) [37]. Table 2 shows that the electrical resistivity decreased considerably from a value of 5.76×10^2 Ω cm for undoped RuO_2 to 1.91×10^2 Ω cm for a 1.00 mol% cobalt-doped RuO_2 electrode. For a given temperature, the electrical resistivity decreases with increasing cobalt-doping level up to 1.00 mol%. This is because of substitution of ruthenium(III) by cobalt(II), which is also evident from the XRD data. Cobalt has only two electrons that form a covalent bond with oxygen. There is a deficiency of one electron, which reduces the electrical resistivity. Above a cobalt-doping level of 1.00 mol%, the electrical resistivity increases (2.70×10^2 Ω cm at a cobalt-doping level of 2.00 mol %). Such behaviour points to a change in electrical conduction in RuO_2 from n-type to p-type [38] with increasing cobalt doping.

The logarithmic dependency of electrical resistivity on inverse of temperature provides activation energy (Ea) [39]. The activation energies are 0.037–0.047 eV and 0.041–0.054 eV (Table 2) in the low-temperature and high-temperature regions, respectively. The activation energies are different for different cobalt-doping levels, confirming that the cobalt-doped electrodes each have different levels of oxygen vacancies [38]. These activation energies are lower than the value of 0.45–0.48 eV reported by Ugur and coworkers [40].

3.6. Electrochemical

In the light of the foregoing results, the cobalt-doped RuO_2 electrodes were subjected to electrochemical tests such as CV, GCD and EIS in a 0.5

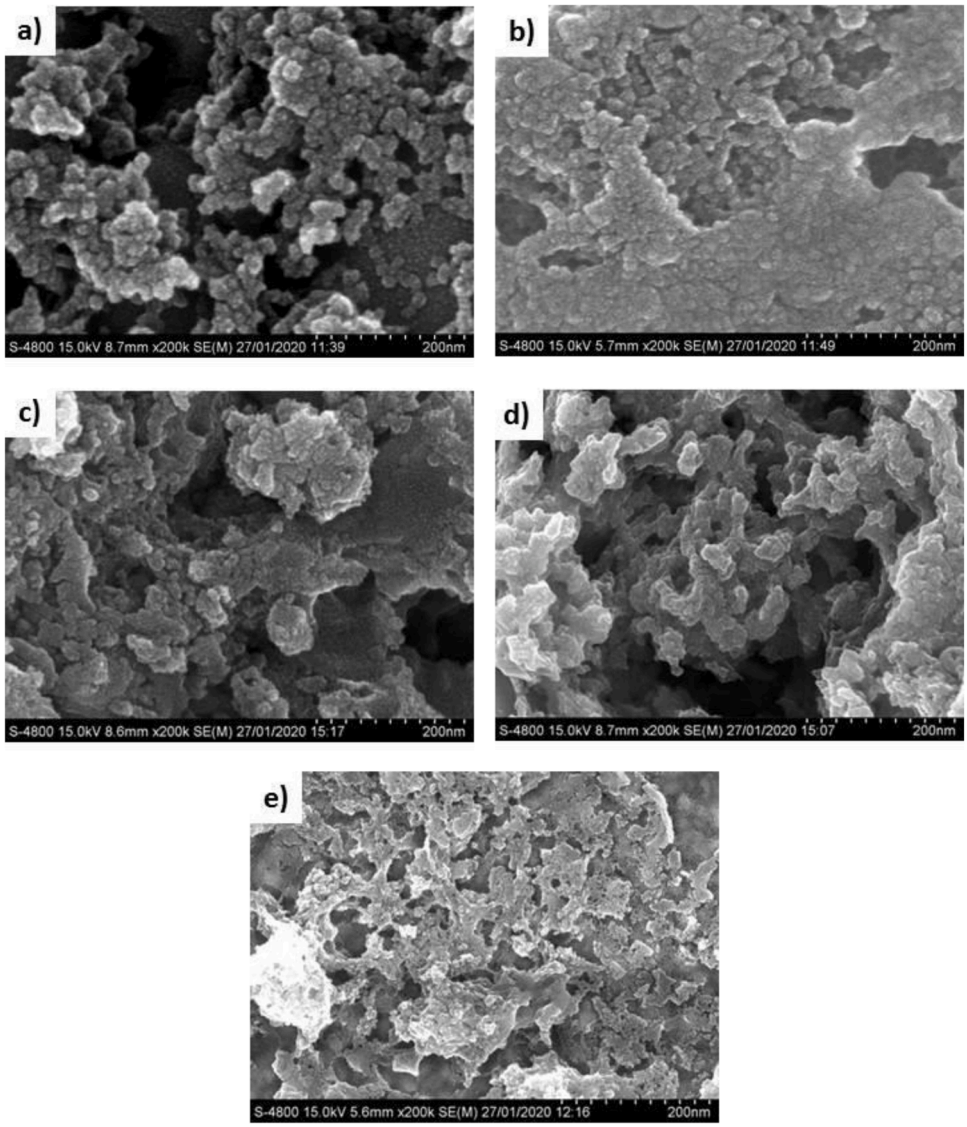

Fig. 3. FESEM images (magnification 200,000 ×) of cobalt doped RuO_2 films with various cobalt-doping contents (a) undoped (Rutile) (b) 0.25 mol%, (c) 0.50 mol% (d) 1.00 mol%, and (e) 1.50 mol%, respectively.

M H_2SO_4 electrolyte with a three-electrode setup.

3.6.1. CV

CV is an effective measurement to determine the capacitive behaviour of materials. Fig. 6 shows the effect of the scan rate on CV curves between 0 V and 1.0 V in a 0.5 M H_2SO_4 electrolyte. Overall, the current density is enhanced with rise in scan rate used to perform CV analysis. The good current responses and nearly symmetric CV curves in the cathodic and anodic paths indicate that the electrodes display robust supercapacitive behaviour. It can be seen from Fig. 6 that the area under the CV curve of the 1.00 mol% cobalt-doped RuO_2 electrode (Fig. 6 (d)) is greater than the areas under the curves of undoped and 0.25 mol%, 0.50 mol%, 1.50 mol%, and 2.00 mol% cobalt-doped RuO_2 electrodes (Fig. 6 (a-c) (e-f)). This suggests that the 1.00 mol% cobalt-doped RuO_2 electrode can store more charge and that its electrochemical performance is superior. The greater area under the CV curve is due to the porous surface morphology, seen under FESEM (Fig. 3), and the strong electrical conductivity (Fig. 5; Table 2), which increases the diffusion of the ions of H_2SO_4. Fig. 7 (a) shows the CVs recorded at 10 mV s^{-1} for undoped and cobalt-doped RuO_2 electrodes. The specific capacitances of RuO_2 electrodes were determined from the CV curves using a relation given elsewhere [41] (Table 3). Fig. 7 (b) shows the variation of specific capacitance with scan rate. The 1.00 mol% cobalt-doped RuO_2 electrode displayed the highest specific capacitance (1072 F g^{-1} at a 5 mV s^{-1} scan rate), followed by the 1.50 mol% cobalt-doped RuO_2 electrode (1045 F g^{-1} at a 5 mV s^{-1} scan rate). These values are much higher than that of the undoped RuO_2 electrode (893 F g^{-1} at a 5 mV s^{-1} scan rate). The rise in specific capacitance with cobalt-doping level is due to a decreased crystallite size (Table 1) and improved electrical conductivity (Table 2), as a result of which there are more active sites for energy storage [42]. The reduction in specific capacitance with an increase in cobalt-doping level beyond 1.00 mol% is due to decreased electrical conductivity of cobalt-doped RuO_2 electrode (Table 2) and a decreasing path for diffusion of electrolyte ions. This shows that cobalt doping considerably raises the specific capacitance of RuO_2.

3.6.2. GCD

Fig. 8 (a-f) shows the charge–discharge curves of the electrodes at current densities of 0.5 A g^{-1}, 1.0 A g^{-1}, 2.0 A g^{-1}, and 4.0 A g^{-1} in the potential window from 0 V to 0.85 V in 0.5 M H_2SO_4. It can be seen from the curves that the discharge time decreases with increasing charge–discharge current density, following this equation [43]:

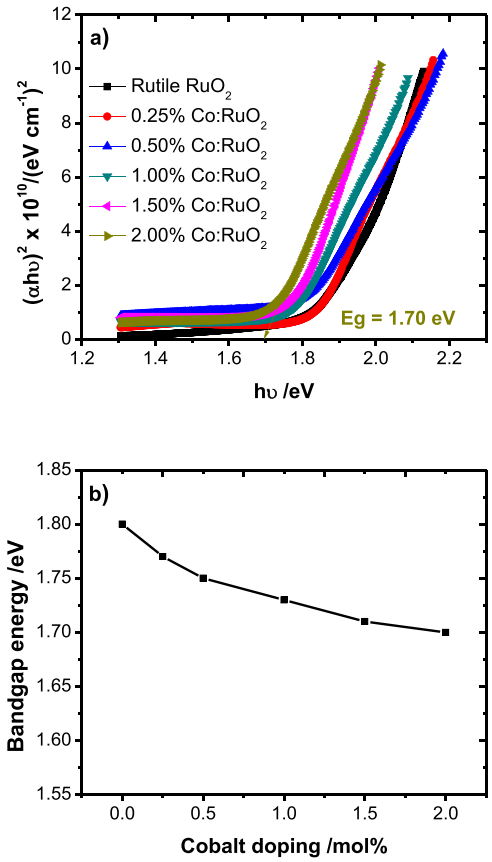

Fig. 4. **(a)** Plot of $(\alpha h\nu)^2$ versus $h\nu$ and (b) Variation of bandgap energy with cobalt doping content for spray deposited cobalt doped RuO_2.

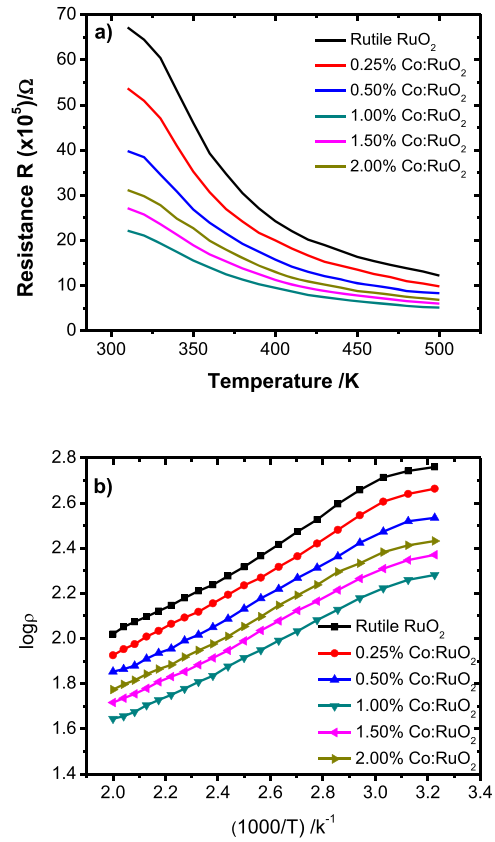

Fig. 5. (a) Temperature dependent contact resistances and (b) Variation of logρ vs 1000/T for spray deposited cobalt doped RuO_2 measured by the four-point probe technique.

Table 2
Optical and electrical properties of cobalt doped RuO_2 spray deposited with various cobalt-doping contents.

Cobalt doping content (mol%)	Band gap (eV)	Electrical resistivity (Ωcm) 310K (× 10^2)	500K (× 10^2)	Activation energy (eV) LT	HT
Undoped	1.80	5.76	1.05	0.045	0.051
0.25	1.77	4.61	0.84	0.047	0.054
0.50	1.75	3.43	0.71	0.043	0.041
1.00	1.73	1.91	0.44	0.039	0.041
1.50	1.71	2.35	0.52	0.040	0.045
2.00	1.70	2.70	0.59	0.037	0.045

LT- Low temperature; HT- High temperature.

$$C = \frac{I \times \Delta t}{m \times \Delta V} \quad (1)$$

I is the charge–discharge current at discharge time t (seconds), ΔV is the potential window, and m is the mass of the RuO_2 deposited. Table 4 shows the specific capacitances calculated using Eq. (1) for cobalt-doped RuO_2.

The undoped RuO_2 electrode has a specific capacitance of 964 F g^{-1} at 0.5 A g^{-1}. The specific capacitance increases as the cobalt-doping level of the RuO_2 electrodes increases and becomes highest (1158 F g^{-1} at 0.5 A g^{-1}) with a doping level of 1.00 mol%. This behaviour can be due to the fact that the 1.00 mol% cobalt-doped RuO_2 electrode provides more active sites, increasing the ionic conductivity and diffusion of electrolyte ions in the RuO_2 electrode [44]. Another reason is that the optimum doping of cobalt at 1.00 mol% improves the electronic structure of the RuO_2 electrode, enhancing the electrical conductivity. The specific capacitance decreases when the doping level increases further, becoming 1099 F g^{-1} at 0.5 A g^{-1} (2.00 mol% cobalt-doped RuO_2). These values of the specific capacitance are close to or higher than those reported in the literature for RuO_2 [17,18,20–23,45,46].

Fig. 9 (a) shows the GCD curves of the cobalt-doped RuO_2 electrodes at a current density of 1 A g^{-1}. The linear shape of the charge–discharge curve points to the excellent capacitive properties cobalt-doped RuO_2 electrodes. Considering the charging and discharging times, the cobalt-doped RuO_2 electrodes appear to have excellent coulombic efficiency. Fig. 9 (b) shows a plot of specific capacitance versus current density for cobalt-doped RuO_2 electrodes. The specific capacitance of the 1.00 mol % cobalt-doped RuO_2 electrode reduces from 1158 F g^{-1} at 0.5 A g^{-1} to 957 F g^{-1} at 4.0 Ag^{-1}. Because of the solid electrolyte interface, the specific capacitance is retained to an extent of 82.64%, with only a 17.36% loss.

The specific energy is plotted against the specific power to assess the suitability of cobalt-doped RuO_2 electrodes for use in energy storage devices (Ragone plot, Fig. 10(a)). The specific power and specific energy of the 1.00 mol% cobalt-doped RuO_2 electrode are 1.702 kW kg^{-1} and 96.02 W h kg^{-1}, respectively. These values are better than the values of 151 W kg^{-1} and 3.57 W h kg^{-1} reported by Patil and co-workers [47] for hydrous RuO_2.

GCD tests (1000 charge–discharge cycles) were performed at a current density of 4.0 A g^{-1}. The cycle stability of the 1.00 mol% cobalt-doped RuO_2 electrode is shown in Fig. 10(b). 94.04% of the initial capacitance of the RuO_2 electrode cobalt-doped at a level of 1.00 mol% is sustained, exhibiting superior stability. The inset of Fig. 10(b) shows the GCD curves of the first five cycles. Loss of the active material of the cobalt-doped RuO_2 electrode through dissolution or detachment is what causes the specific capacitance to decrease with the number of cycles [48].

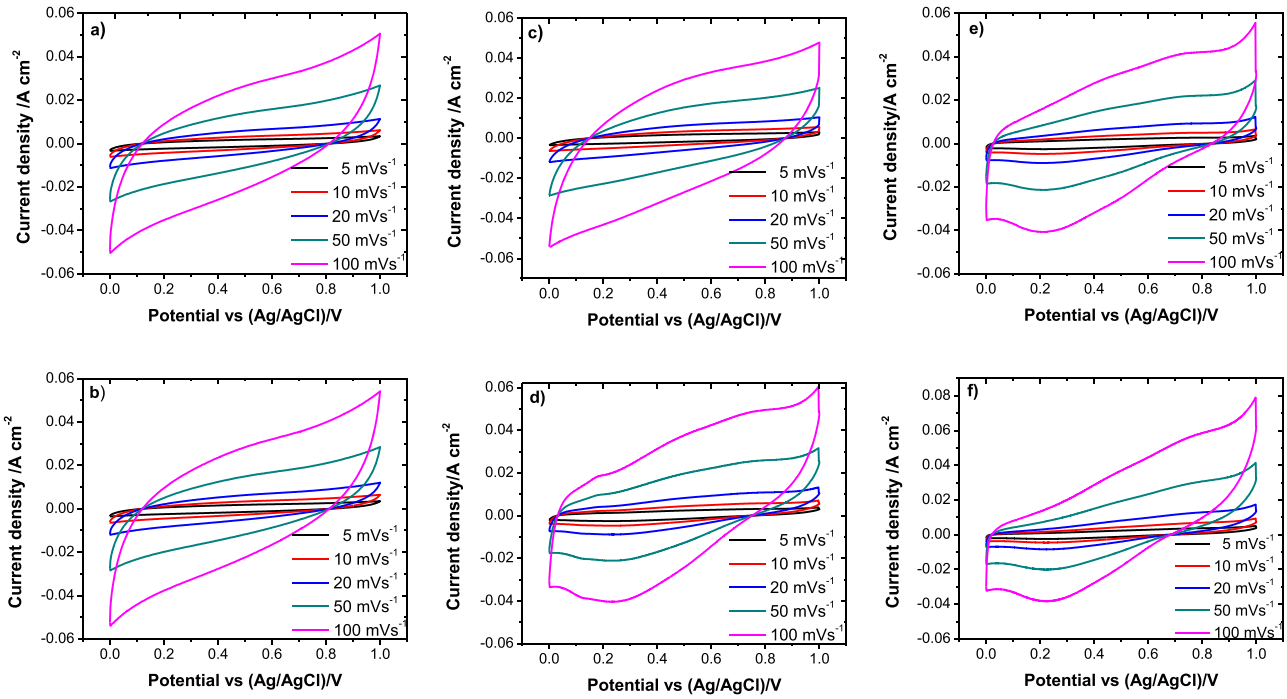

Fig. 6. The CVs at various scan rates for cobalt doped RuO_2 electrodes spray deposited with various cobalt doping contents (a) undoped (Rutile) (b) 0.25 mol%, (c) 0.50 mol% (d) 1.00 mol%, (e) 1.50 mol%, and (f) 2.00 mol%, respectively.

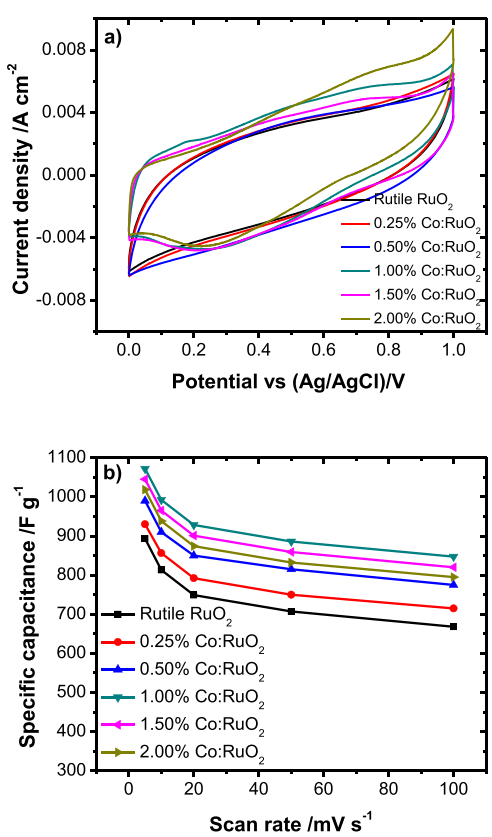

Fig. 7. (a) CVs (scan rate 10 mVs^{-1}) for cobalt doped RuO_2 electrodes spray deposited with various cobalt doping contents, and (b) Plot of specific capacitance versus scan rate for cobalt doped RuO_2 electrodes spray deposited with various cobalt doping contents.

Table 3
Specific capacitance at different scan rates from CV for RuO_2 electrodes spray deposited with various cobalt-doping contents.

Cobalt doping content (mol %) →	undoped	0.25	0.50	1.00	1.50	2.00
Scan rate (mVs^{-1})↓	Specific capacitance from CV (Fg^{-1})					
5	893	930	990	1072	1045	1018
10	813	856	910	992	965	938
20	749	792	850	928	901	874
50	707	750	815	886	859	832
100	668	715	775	847	820	795

3.6.3. EIS

The EIS results (Fig. 11 (a)) were analysed to study the electrochemical kinetics of the cobalt-doped RuO_2 electrodes. All of the cobalt-doped RuO_2 electrodes' Nyquist plots show a depressed semicircle, which denotes a charge-transfer mechanism. The EIS data can be fitted by an equivalent circuit shown in Fig. 11 (b) [41]. The elements in the equivalent circuit are solution resistance (Rs), the charge-transfer resistance (Rct), the double-layer capacitance (Cdl), the Warburg diffusion element (Wo), and the pseudocapacitance element (Cpseudo). The semicircle of the 1.00 mol% cobalt-doped RuO_2 electrode has a smaller radius compared with those of the other electrodes (0.25 mol%, 0.50 mol%, 1.50 mol%, and 2.00 mol%), which indicates that the solution resistance (0.27 Ω) and charge transfer resistance (8.15 Ω cm^2) are the lowest values. This in turn implies a fast charge-transfer rate at the RuO_2 electrode/H_2SO_4 electrolyte interface.

Table 5 presents the Nyquist data of the undoped and cobalt-doped RuO_2 electrodes. In the low-frequency region, the slope of the Nyquist plot shows the diffusion capacity of the H_2SO_4 electrolyte into the undoped and cobalt-doped RuO_2 electrodes. It is clear that the ion diffusion rate of the 1.00 mol% cobalt-doped RuO_2 electrode is greater than those of the undoped electrode and other (0.25 mol%, 0.50 mol%, 1.50 mol%, and 2.00 mol%) cobalt-doped RuO_2 electrodes implying good electrical conductivity [49].

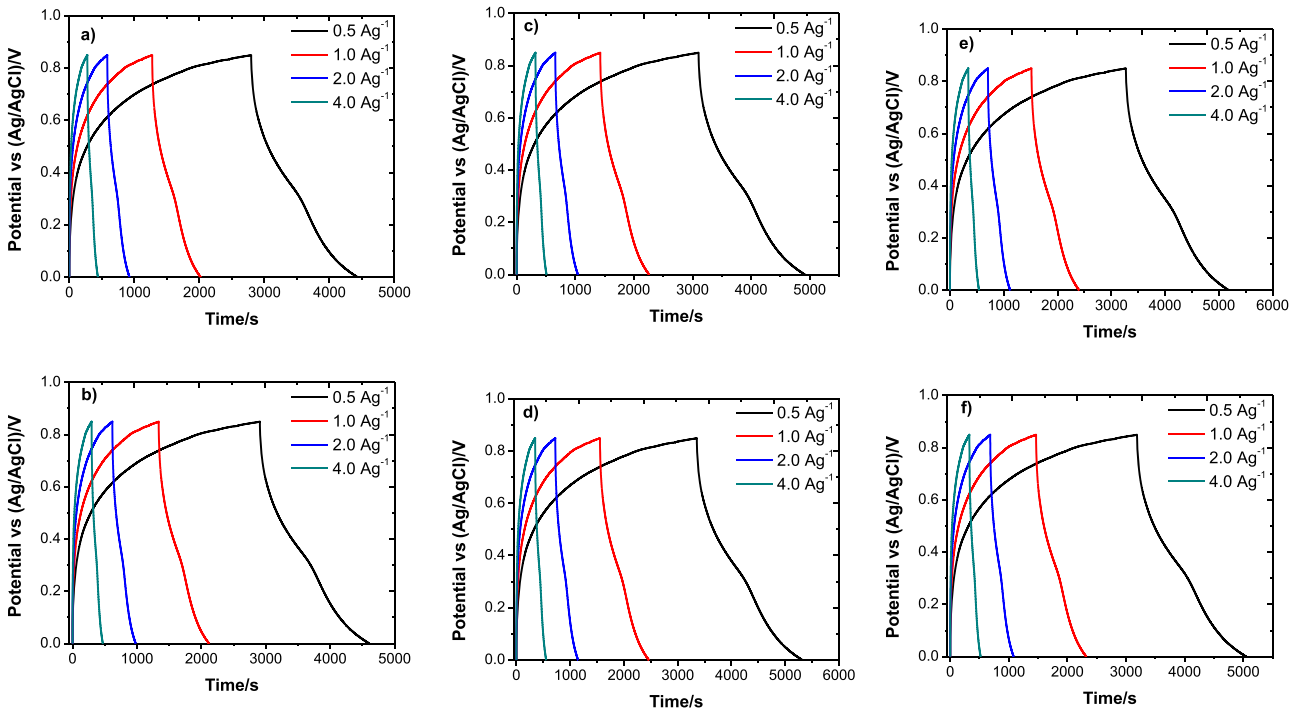

Fig. 8. The GCD curves at various current densities for cobalt doped RuO_2 electrodes spray deposited with various cobalt doping contents (a) undoped (Rutile) (b) 0.25 mol%, (c) 0.50 mol% (d) 1.00 mol%, (e) 1.50 mol%, and (f) 2.00 mol%, respectively.

Table 4
Specific capacitances from GCD for RuO_2 electrodes spray deposited with various cobalt-doping contents.

Cobalt doping content (mol%) →	Undoped	0.25	0.50	1.00	1.50	2.00
Current density (Ag^{-1}) ↓	Specific capacitance from GCD (Fg^{-1})					
0.5	964	1004	1069	1158	1129	1099
1	878	924	983	1071	1042	1013
2	809	855	918	1002	973	944
4	764	810	880	957	928	899

4. Conclusion

Cobalt-doped RuO_2 electrodes were spray deposited with varying cobalt content in the precursor solution. The undoped and cobalt-doped RuO_2 exhibited a rutile tetragonal crystal structure with the P42 space group. The crystallite size was estimated to be 13–9 nm, depending on the cobalt-doping content in the RuO_2. The porous structure and homogeneity of the RuO_2 increased with increasing cobalt-doping content. FESEM images showed a granular and tightly packed morphology without aggregation of grains. The optical bandgap of the spray-deposited undoped RuO_2 electrode was 1.80 eV, and when the cobalt-doping content was increased, the optical bandgap decreased to 1.7 eV. Electrochemical supercapacitive measurements showed that 1.00 mol% cobalt-doped RuO_2 has an exceptionally high specific capacitance of 1072 F g^{-1} at a 5 mV s^{-1} scan rate; in comparison, the corresponding value of an undoped RuO_2 electrode was 893 F g^{-1} at the same scan rate. The increase in specific capacitance is attributed to a more porous morphology and an increased electrical conductivity. This study demonstrates that elemental doping is an efficient way to enhance the electrochemical supercapacitive performance of RuO_2 and that elemental doping can be achieved using chemical spray pyrolysis.

CRediT author statement

All authors contributed to the study conception and design. All

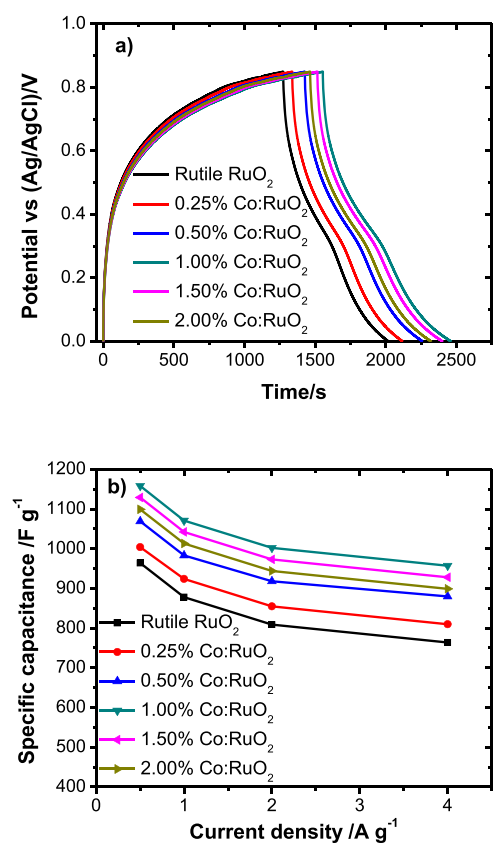

Fig. 9. (a) GCD curves at current density of $1Ag^{-1}$ and (b) plot of specific capacitance versus current density for cobalt doped RuO_2 electrodes spray deposited with various cobalt-doping contents in precursor solution.

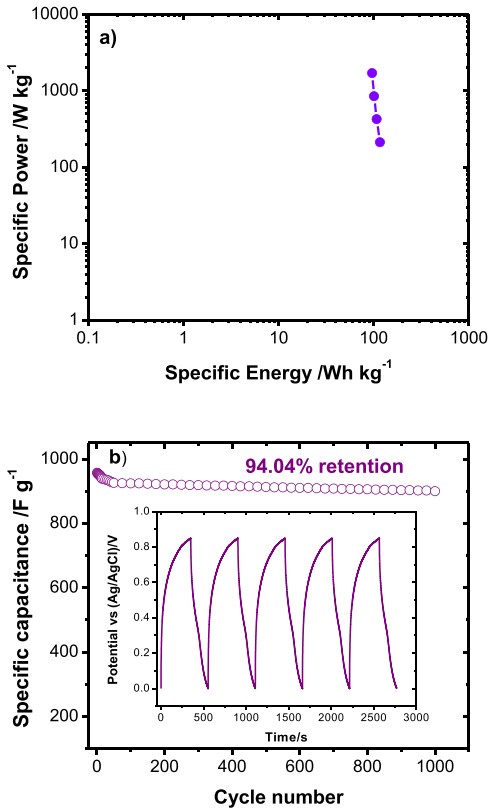

Fig. 10. (a) Ragone plot of spray deposited RuO_2 electrode doped with 1.00 mol% cobalt contents, (b) Long term cycling performance at the current density of $4Ag^{-1}$ for spray deposited RuO_2 electrode with 1.00 mol% cobalt doping contents. The inset shows the charge-discharge curves of the first 5 cycles.

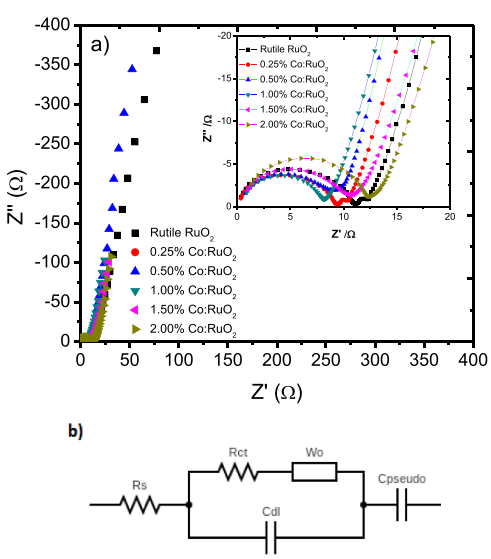

Fig. 11. Nyquist plot for RuO_2 electrodes spray deposited with various cobalt-doping contents. The inset is the enlarged Nyquist plots in high frequency region and (b) equivalent circuit diagram proposed for analysis of the EIS data.

authors performed material preparation, data collection and analysis. The first draft of the manuscript was written by Chandrashekhar R., and Dr Abhijit Yadav commented on previous versions of the manuscript. All authors read and approved the final manuscript.

Table 5
Nyquist data for RuO_2 electrodes spray deposited with various cobalt-doping contents.

Cobalt doping content (mol%)	Rs (Ω)	Rct (Ωcm^2)
undoped	0.32	11.38
0.25	0.30	09.58
0.50	0.29	09.03
1.00	0.27	08.15
1.50	0.31	11.25
2.00	0.34	12.62

Declaration of Competing Interest

The authors declare that they have no known competing financial interests or personal relationships that could have appeared to influence the work reported in this paper.

Data availability

No data was used for the research described in the article.

References

[1] H. Gonenc, B. Scholtens, Environmental and financial performance of fossil fuel firms: a closer inspection of their interaction, Ecol. Econ. 132 (2017) 307–328.
[2] Rafael J. Silva, Vanessa Klobukoski, Jessica I.S. de Paula, Izabel C. Riegel-Vidotti, Marcio Vidotti, Assembly of symmetric supercapacitor based on alginate hydrogel electrolyte and polyaniline modified electrodes, Electrochim. Acta 429 (2022), 140914.
[3] Jun Zhang, Rui Huang, Zhenbiao Dong, Hualin Lin, Sheng Han, An illumination-assisted supercapacitor of rice-like CuO nanosheet coated flexible carbon fiber, Electrochim. Acta (2022), 140789.
[4] Shuai Liu, Li Wei, Huai Wang, Review on reliability of supercapacitors in energy storage applications, Appl. Energy 278 (2020), 115436.
[5] Aneeya Samantara, Daisuke Tashima, Supercapacitors for the Next Generation, IntechOpen Publishers, 2022.
[6] T. Schoetz, L.W. Gordon, S. Ivanov, A. Bund, D. Mandler, R.J. Messinger, Disentangling faradaic, pseudocapacitive, and capacitive charge storage: a tutorial for the characterization of batteries, supercapacitors, and hybrid systems, Electrochim. Acta 412 (2022), 140072.
[7] Zuozhao Zhai, Lihui Zhang, Tianmin Du, Bin Ren, Yuelong Xu, Shasha Wang, Junfeng Miao, Zhenfa Liu, A review of carbon materials for supercapacitors, Mater. Des. 221 (2022), 111017.
[8] Cuiqin Fang, Dong Zhang, High multifunctional performance structural supercapacitor with Polyethylene oxide cement electrolyte and reduced graphene oxide@$CuCo_2O_4$ nanowires, Electrochim. Acta 401 (2022), 139491.
[9] Navajsharif S. Shaikh, Shivaji B. Ubale, Vikas J. Mane, Jasmin.S. Shaikh, Vaibhav. C. Lokhande, Supareak Praserthdam, Chandrakant D. Lokhande, Pongsakorn Kanjanaboos, Novel electrodes for supercapacitor: conducting polymers, metal oxides, chalcogenides, carbides, nitrides, MXenes, and their composites with graphene, J. Alloys Compd. 893 (2022), 161998.
[10] José G. Ruiz-Montoya, Lady V. Quispe-Garrido, J.C. Calderón Gómez, Angélica M. Baena-Moncada, Josué M. Gonçalves, Recent progress in and prospects for supercapacitor materials based on metal oxide or hydroxide/biomass-derived carbon composites, Sustain. Energy Fuels 5 (2021) 5332–5365.
[11] C.D. Lokhande, D.P. Dubal, Oh-Shim Joo, Metal oxide thin film based supercapacitors, Curr. Appl. Phys. 11 (2011) 255–270.
[12] P. Simon, Y. Gagotsi, Materials for electrochemical capacitors, Nat. Mater. 7 (2008) 845–854.
[13] Saira Ishaq, Mahmoud Moussa, Farah Kanwal, Raheel Ayub, Truc NgoVan, Umar Azhar, Dusan Losic, One step strategy for reduced graphene oxide/cobalt-iron oxide/polypyrrole nanocomposite preparation for high performance supercapacitor electrodes, Electrochim. Acta 427 (2022), 140883.
[14] Murat Ates, Carlos Fernandez, Ruthenium oxide–carbon-based nanofiller-reinforced conducting polymer nanocomposites and their supercapacitor applications, Polym. Bull. 76 (2019) 2601–2619.
[15] Dongfang Yang, Pulsed laser deposition of cobalt-doped manganese oxide thin films for supercapacitor applications, J. Power Sources 198 (2012) 416–422.
[16] Mariam Hasan, Sidra Zawar, Ghulam M. Mustafa, Abdul Ghaffar, Aamir Razaq, Shahid Atiq, Porous Architecture of Ni substituted $ZnMn_2O_4$ nanospheres as an electrode material for supercapacitor applications, Phys. B 633 (2022), 413767.
[17] Koshal Kishor, Sulay Saha, Alhad Parashtekar, Raj Ganesh S Pala, Increasing Chlorine Selectivity through Weakening of Oxygen Adsorbates at Surface in Cu Doped RuO_2 during Seawater Electrolysis, J. Electrochem. Soc. 165 (2018) J3276–J3280.
[18] P.S. Joshi, D.S. Sutrave, Mn doped ruthenium oxide permeable structures and their electrochemical properties, Elixir Mater. Sci. 105 (2017) 46136–46140, 46136.

[19] Kateřina Minhová Macounová, Nina Simic, Elisabet Ahlberg, Petr Krtil, Hypochlorite oxidation on RuO_2-based electrodes: a combined electrochemical and *in situ* mass spectroscopic study, Electrocatalysis 10 (2019) 45–55.
[20] Valery Petrykin, Kateřina Macounová, Maki Okube, Sanjeev Mukerjee, Petr Krtil, Local structure of Co doped RuO_2 nanocrystalline electrocatalytic materials for chlorine and oxygen evolution, Catal. Today 202 (2013) 63–69.
[21] Jianwei Su, Ruixiang Ge, Kemin Jiang, Yan Dong, Fei Hao, Ziqi Tian, Guoxin Chen, Liang Chen, Assembling ultrasmall copper-doped ruthenium oxide nanocrystals into hollow porous polyhedra: highly robust electrocatalysts for oxygen evolution in acidic media, Adv. Mater. (2018), 1801351.
[22] Yiyi Wu, Muhammad Tariq, Waqas Qamar Zaman, Wei Sun, Zhenhua Zhou, Ji Yang, Bimetallic doped RuO_2 with manganese and iron as electrocatalysts for favorable oxygen evolution reaction performance, ACS Omega 5 (2020) 7342–7347.
[23] Thomas I. Valdez, Keith J. Billings, Jeff Sakamoto, Florian Mansfeld, S. R. Narayanan, Iridium and lead doped ruthenium oxide catalysts for oxygen evolution, ECS Trans. 25 (1) (2009) 1371–1382.
[24] JCPDS card no. 88-0322.
[25] J.S. Revathy, N.S. Chitra Priya, K. Sandhya, Deepthi N. Rajendran, Structural and optical studies of cerium doped gadolinium oxide phosphor, Bull. Mater. Sci. 44 (2021) 13.
[26] A.A. Yadav, M.A. Barote, T.V. Chavan, E.U. Masumdar, Influence of indium doping on the properties of spray deposited $CdS_{0.2}Se_{0.8}$ thin films, J. Alloys Compd. 509 (2011) 91–921.
[27] A.P. Jadhav, J.H. Oh, S.W. Park, H. Choi, B.K. Moon, B.C. Choi, K. Jang, J. H. Jeong, S.S. Yi, J.H. Kim, Enhanced down and upconversion emission for Li^+ co-doped Gd_2O_3:Er^{3+} nanostructures, Curr. Appl. Phys. 16 (2016) 1374–1381.
[28] Daniel F. Abbott, Valery Petrykin, Maki Okube, Zdenk Bastl, Sanjeev Mukerjee, Petr Krtil, Selective chlorine evolution catalysts based on Mg-doped nanoparticulate ruthenium dioxide, J. Electrochem. Soc. 162 (1) (2015) H23–H31.
[29] Yuying Yang, Yarong Liang, Yadi Zhang, Ziyu Zhang, Zhiming Li, Zhongai Hu, Three-dimensional graphene hydrogel supported ultrafine RuO_2 nanoparticles for supercapacitor electrodes, New J. Chem. 39 (2015) 4035–4040.
[30] Nikola Lenar, Beata Paczosa-Bator, Robert Piech, Ruthenium dioxide nanoparticles as a high-capacity transducer in solid-contact polymer membrane-based pH-selective electrodes, Microchim. Acta 186 (2019) 777.
[31] A.A. Yadav, M.A. Barote, E.U. Masumdar, Studies on cadmium selenide (CdSe) thin films deposited by spray pyrolysis, Mater. Chem. Phys. 121 (2010) 53–57.
[32] Silan Baturay, Ahmet Tombak, Derya Kaya, Yusuf Selim Ocak, Murat Tokus, Murat Aydemir, Tahsin Kilicoglu, Modification of electrical and optical properties of CuO thin films by Ni doping, J. Sol-Gel Sci. Technol. 78 (2016) 422–429.
[33] Antonino Gulino, Giuseppe Compagnini, A.A. Scalisi, Large third-order nonlinear optical properties of cadmium oxide thin films, Chem. Mater. 15 (2003) 3332–3336.
[34] A. Belkind, Z. Orban, J.L. Vossen, J.A. Woollam, Optical properties of RuO_2 films deposited by reactive sputtering, Thin Solid Films 207 (1992) 242–247.
[35] Farid El-Tantawy, Ahmed A. Al-Ghamdi, Attieh A. Al-Ghamdi, Yusuf A. Al-Turki, Ahmed Alshahrie, Faten Al-Hazmi, Omar A. Al-Hartomy, Optical properties of nanostructured ruthenium dioxide thin films via sol-gel approach, J. Mater. Sci. Mater. Electron. 28 (2017) 52–59.
[36] V.D. Patake, C.D. Lokhande, Chemical synthesis of nano-porous ruthenium oxide (RuO_2) thin films for supercapacitor application, Appl. Surf. Sci. 254 (2008) 2820–2824.
[37] A.A. Yadav, Physical and electrochemical properties of spray deposited Co_3O_4 thin films, Phase Transit 94 (10) (2021) 691–704.
[38] A R Bally, E N Korobeinikova, P E Schmid, F Levy, F Bussy, Structural and electrical properties of Fe-doped TiO_2 thin films, J. Phys. D: Appl. Phys. 31 (1998) 1149–1154.
[39] Nandkishor Manoharrao Patil, Santosh G. Nilange, Vidyadevi A. Jundale, Pratibha B. Kadam, R. Chandrashekhar, Abhijit A. Yadav, Structural, optical and electrical properties of spray-deposited Fe-doped nanocrystalline $ZnS_{0.2}Se_{0.8}$ thin films, Phase Transit 94 (2021) 493–510.
[40] D. Ugur, A.J. Storm, R. Verberk, J.C. Brouwer, W.G. Sloof, Kinetics of Reduction of a RuO_2(110) Film on Ru(0001) by H_2, J. Phys. Chem. C 116 (2012) 26822–26828.
[41] A.A. Yadav, S.N. Jadhav, D.M. Chougule, P.D. Patil, U.J. Chavan, Y.D. Kolekar, Spray deposited Hausmannite Mn_3O_4 thin films using aqueous/organic solvent mixture for supercapacitor applications, Electrochim. Acta 206 (2016) 134–142.
[42] Zhongxing Wang, Jiliang Zhu, Ping Sun, Pengyu Zhang, Zifan Zeng, Shuang Liang, Xiaohong Zhu, Nanostructured Mn–Cu binary oxides for supercapacitor, J. Alloys Compd. 598 (2014) 166–170.
[43] A.A. Yadav, U.J. Chavan, Electrochemical supercapacitive performance of spray deposited $NiSnO_3$ thin films, Thin Solid Films 634 (2017) 33–39.
[44] Shanshan Xiong, Shuting Wenga, Yu Tang, Lei Qian, Yanqiu Xu, Xianfa Li, Hongjun Lin, Yanchao Xu, Yang Jiao, Jianrong Chen, Mo-doped Co_3O_4 ultrathin nanosheet arrays anchored on nickel foam as a bi-functional electrode for supercapacitor and overall water splitting, J. Colloid Interface Sci. 602 (2021) 355–366.
[45] Sujoy Sarkar, Debdyuti Mukherjee, R. Harini, G. Nagaraju, Ionic liquid-assisted synthesis of tri-functional ruthenium oxide nanoplatelets for electrochemical energy applications, J. Mater. Sci. 57 (2022) 7680–7693.
[46] Sujit Kumar Mondal, N. Munichandraiah, Anodic deposition of porous RuO_2 on stainless steel for supercapacitor studies at high current densities, J. Power Sources 175 (2008) 657–663.
[47] U.M. Patil, S.B. Kulkarni, V.S. Jamadade, C.D. Lokhande, Chemically synthesized hydrous RuO_2 thin films for supercapacitor application, J. Alloys Comp. 509 (2011) 1677–1682.
[48] D.P. Dubal, A.D. Jagadale, S.V. Patil, C.D. Lokhande, Simple route for the synthesis of supercapacitive Co–Ni mixed hydroxide thin films, Mater. Res. Bull. 47 (2012) 1239–1245.
[49] H. Tang, J. Wang, H. Yin, H. Zhao, D. Wang, Z. Tang, Growth of polypyrrole ultrathin films on MoS_2 monolayers as high-performance supercapacitor electrodes, Adv. Mater. 27 (6) (2015) 1117–1123.